

Optical and Radar Observations of the February 2025 Falcon 9 Upper-Stage Re-entry

Juha Vierinen^{1,2}, Dabrowka Knach¹, Jorge L. Chau², Gerd Baumgarten², Devin Huyghebaert², Matthias Clahsen², Nico Pfeffer², Toralf Renkwitz², Robin Wing², Kenneth S. Obenberger³, Björn Gustavsson¹, and Daniel Kastinen⁴

¹Department of Physics and Technology, UiT The Arctic University of Norway, Tromsø, Norway

²Leibniz Institute of Atmospheric Physics at the University of Rostock, Kühlungsborn, Germany

³Space Warfare Directorate, Air Force Research Laboratory, Kirtland Air Force Base, New Mexico, USA

⁴Swedish Institute of Space Physics, Kiruna, Sweden

Abstract. We investigate the February 19, 2025, re-entry of a Falcon 9 upper stage using optical observations from 43 meteor cameras across central Europe together with radar detections of re-entry plasma obtained with the 32.55 MHz SIMONE Germany multistatic radar system. Optical observations of fragment emissions between 85 and 36 km altitude were used to reconstruct 30 fragment trajectories, identify two main fragment families, and fit ballistic trajectories to estimate kinetic energy loss per unit mass. The optical detection-height distribution peaks near 60 km with a standard deviation of 10 km, and both optical and radar signatures occur in the same broad altitude region as the maximum kinetic-energy loss. Radar echoes were detected at altitudes between 55 and 75 km, and the radar-derived positions are consistent with those obtained from optical observations. Two distinct radar echo types associated with the re-entry plasma were identified: (1) specular trail echoes from overdense wake plasma, with radar cross-sections (RCS) of up to 60 dBsm, and (2) short-lived non-specular trail echoes with RCS values of 20–30 dBsm, exhibiting a delay of 1–2 s compared to optical signatures. The characteristic decay time of both echo types is approximately 1 s. In the radar-echo altitude range, the estimated Knudsen numbers for meter-scale fragments are well below unity, consistent with continuum-flow conditions and shock-driven plasma production rather than ordinary meteor-like impact ionization. These serendipitous radar observations demonstrate that the atmospheric re-entry of other spacecraft, including objects smaller than the Falcon 9 upper stage such as Starlink satellites, may likewise be detectable using comparable multistatic meteor radar systems deployed globally.

1 Introduction

The rapid commercialization of space has transformed Earth’s orbital environment. Rising launch rates, large satellite constellations, and expanded ride-share missions have substantially increased the number, mass, and surface area of objects in low Earth orbit (LEO). Many of these objects orbit at altitudes where atmospheric drag causes orbital decay within years. Projected growth in space activity could increase the annual rate of atmospheric re-entries by a factor of 2 to 3 over the next decade (ESA, 2025), creating an urgent need for improved understanding of re-entry processes, deposition of spacecraft materials impacting atmospheric chemistry and radiative balance, and ground safety risks.

A significant fraction of the mass re-entering the atmosphere originates from spent upper stages of launch vehicles. Falcon 9 and Falcon Heavy upper stages alone accounted for 0.36 kt out of 1.59 kt of spacecraft mass influx to the top of the atmosphere in 2024 (Schulz et al., 2026), making observations of re-entries of these objects valuable, as they represent a significant portion of the re-entry flux. This influx is increasingly important to characterize because ablated spacecraft material can introduce anthropogenic metals into the middle atmosphere, where recent observational and modeling studies suggest they may influence aerosol composition and stratospheric chemistry (Murphy et al., 2023; Wing et al., 2026; Maloney et al., 2025). Although the total annual spacecraft influx of about 1.6 kt corresponds to only about 400 ppt of the total atmospheric mass between 50 and 70 km, its composition rather than its bulk mass may still be important if these materials have unusually high chemical reactivity, catalytic activity, efficient radiative absorption, or unusually long atmospheric lifetimes, many of which remain poorly constrained at present.

In the early hours of 19 February 2025, a Falcon 9 upper stage from the Starlink 11-4 mission underwent an atmospheric re-entry over central Europe. The Polish Space Agency monitored the object because of its orbital inclination of approximately 53° , and predicted that the re-entry trajectory could pass over Poland, posing potential ground hazards. After the event, nine fragments were recovered on the ground and characterized along a strewn field spanning approximately 70 km (Kruzynski et al., 2025).

This event represents a unique opportunity to investigate spacecraft re-entry processes using a multi-instrument dataset. Observations are available from optical all-sky fireball cameras (Hankey et al., 2020), specular radars capable of detecting re-entry plasma (Chau et al., 2022), infrasound sensors (Hupe et al., 2025), as well as resonance lidar observations of Lithium (Wing et al., 2026).

Plasma sheaths around re-entry vehicles have long been studied because they can attenuate or interrupt communications with the ground. Classical studies analyzed radio transmission through lifting-vehicle plasma sheaths (Evans and Huber, 1963) and used Langmuir probes to estimate electron densities surrounding re-entry vehicles (Scharfman and Bredfeldt, 1966). The same ionized flow is also relevant for radar phenomenology, because plasma-clad bodies can exhibit modified scattering behavior (Miller, 1966; Mitchell et al., 1969). While theoretical work exists on radar scattering from sheath plasma for hypervelocity entry vehicles (Mitchell et al., 1969; Cong et al., 2022; Qian et al., 2017; Esposito et al., 2024), observations of re-entering orbital spacecraft remain scarce in the literature. Notable examples are the radio echoes reported during the Mercury MA-6 re-entry (Lin, 1962), airborne radar measurements obtained during the Ariane 5 EPC re-entry (Rubin et al., 2005), and laboratory plasma measurements performed by (Petervari et al., 2026).

On the other hand, a significant body of work exists on observations and modeling of radar echoes associated with meteors. It is known that the plasma created during hypervelocity atmospheric entry of meteors can substantially enhance the radar detectability of the meteoroids, producing meteor head echoes (Close et al., 2007) that are associated with the plasma surrounding the ablating meteoroid, and specular trail echoes that have very large radar cross-sections (RCS) due to the coherent addition of scattered EM waves along an extended Fresnel zone (McKinley, 1961; Poulter and Baggaley, 1977). These radar echoes from meteoric plasma make it possible to detect micrometeoroids entering the Earth's atmosphere using radar, which would not be

sensitive enough to observe echoes from small meteoroid bodies without the significantly larger plasma structure surrounding it.

The objectives of this study are to: (1) reconstruct the three-dimensional trajectories of re-entry fragments using all-sky camera triangulation, (2) fit ballistic trajectories to estimate re-entry dynamics to allow analysis of radar observations, and (3) characterize the radar signatures associated with the re-entry debris.

2 Instrumentation and Data

The two datasets used in this study are optical observations from the AllSky7 meteor camera network (Hankey et al., 2020) and radar observations from the SIMONE (Spread Spectrum Interferometric Multistatic meteor radar Observing Network) Germany multistatic radar system (Chau et al., 2022). Together, they provide complementary information on the re-entry, with the cameras tracking the luminous fragment trajectories and the radar probing the associated plasma signatures. An overview of the observing geometry, detections, recovered ground fragments in Poland reported by Kruzynski et al. (2025), and qualitative projected impact locations is given in Figure 1.

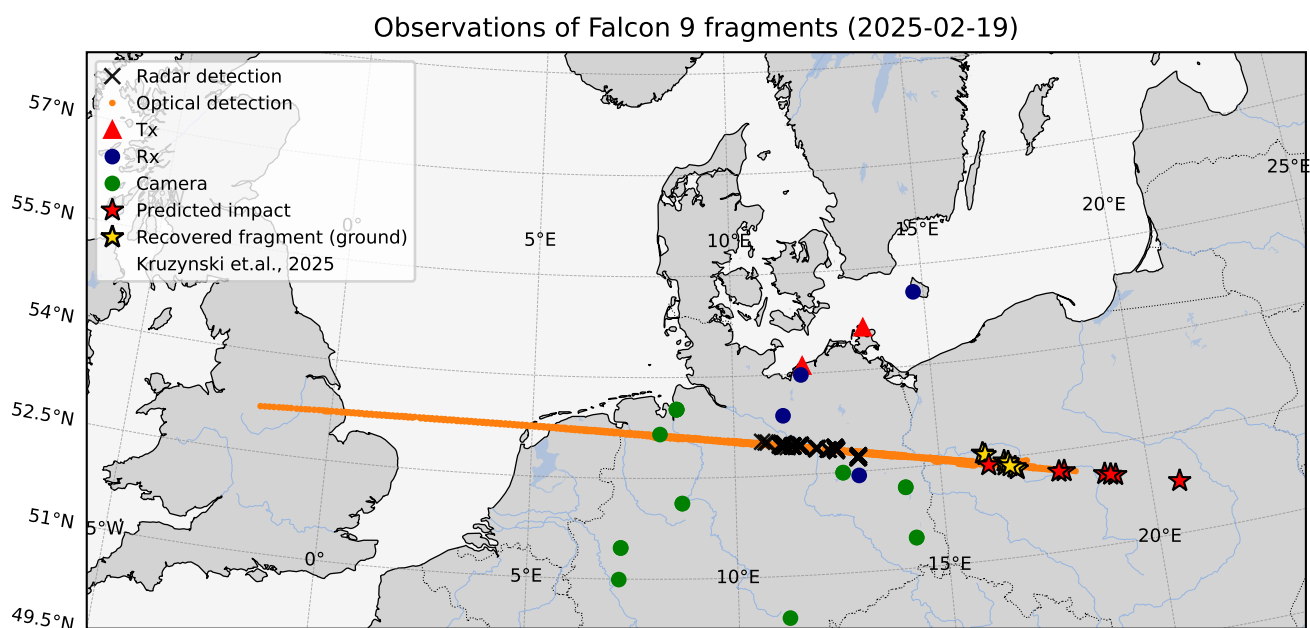


Figure 1. Map of the study area showing SIMONE radar transmitters (triangles), SIMONE radar receivers (circles), optical fragment detections (orange), selected radar detections (black crosses), recovered ground fragments reported by Kruzynski et al. (2025) in Poland (yellow stars), and projected ground fragment locations extrapolated from optical trajectories (red stars). The AllSky7 cameras used in the triangulation are shown with green circles.

2.1 AllSky7 Meteor Camera Network

Fireball camera networks have already shown their value for reconstructing spacecraft re-entries, constraining upper-stage orbits from video observations, and investigating upper-stage fragmentation during re-entry (Peña-Asensio et al., 2021; Bartková et al., 2023). The optical observations analyzed in this study were acquired through the European AllSky7 Fireball Network. Each station consists of a camera system equipped with seven NetSurveillance NVT cameras with the Sony Starvis IMX291 sensor and a 4 mm $f/1.0$ lens, recording at 25 fps. Each camera has a field of view of about $40^\circ \times 85^\circ$. To cover the full sky, five of the cameras are horizontally oriented at an inclination of $\sim 25^\circ$, while the remaining two cameras cover the northern and southern directions at an inclination of $\sim 70^\circ$ (Hankey et al., 2020).

2.2 SIMONe Germany

The radar data analyzed in this work were collected with the SIMONe Germany system, a multistatic specular meteor radar system developed to observe atmospheric winds in the mesosphere and lower thermosphere (Chau et al., 2019; Vierinen et al., 2019) using underdense specular meteor trail echoes with diverse viewing angles. The network comprises two transmitting stations, located in Juliusruh and Kühlungsborn. Each site operates six transmitting antennas that emit independent 1000-bit pseudorandom binary phase-coded continuous-wave signals (Vierinen et al., 2016; Chau et al., 2019) at 32.55 MHz, with a combined transmit power of 3 kW (500 W per antenna). This setup permits interferometric direction finding using single receiver antennas, provides an unaliased total propagation range of 3000 km, and supports an unaliased Doppler shift range of ± 50 kHz. The positions of the transmitters in Juliusruh and Kühlungsborn and the receivers used in this work, i.e., in Bornholm, Bornim, Moitin, and Hagenow, are illustrated in Figure 1.

3 Methods

The AllSky7 meteor camera network measurements were triangulated using dual camera observations to derive the positions of the fragments as a function of time. A ballistic fit of the trajectories was performed to allow the calculation of the energy loss rate and vector velocity along the fragment paths. The SIMONe radar observations were processed to identify the location, Doppler shift, and RCS of the echoes associated with the re-entry debris. The custom data-processing and figure-generation software used in this study is publicly available (Vierinen, 2026a).

3.1 Dual camera triangulation

The optical data processing focused on two main tasks: star calibration and stereoscopic triangulation of fragment positions. The February 19th event was primarily observed from stations in Germany, but one observation from the United Kingdom (AMS101) and two observations from Belgium (AMS67) are also available. Figure 2 shows the time and duration of fragment visibility in each available observation. Pairs of overlapping videos chosen for calibration and triangulation were selected based on video quality, duration, fragment visibility, overlap with other observations, and star visibility. Out of 43 videos, 15 were

calibrated and included for further stereoscopic triangulation. Although AMS101 detected the re-entry at 03:43:00 UTC, no stars were visible in that video to allow calibration, and no additional cameras were available for triangulation at that time.

An average of about 100 stars was identified in most calibrated camera observations with good fragment visibility, enabling accurate plate solving and lens modeling. Star calibration was performed on the same video that contains the re-entry to minimize calibration errors due to camera movement, and star positions were cross-checked during triangulation to detect timing offsets or camera motion. The geometric camera calibration and triangulation were carried out with AIDA_tools (Gustavsson, 2026) and followed the procedures described by Gustavsson et al. (2008) and Vierinen et al. (2022). The camera lens-model calibration residuals were around $\pm 1/4$ pixel.

Figure 3 shows six representative frames from six different cameras, ordered chronologically through the re-entry event. Together, the panels illustrate the evolution of the fragmentation from the early phase of the breakup to the final visible fragments near the end of the event. Assigned fragment identifiers are labeled on the plot.

Fragments were located and triangulated using pairs of calibrated videos. Videos recorded at 25 fps were sampled at 1 s intervals (every 25th frame) for the triangulation runs. Detected fragments were assigned identifiers using the ranges 1–9 and a–z. For each detection, we stored an entry in Hierarchical Data Format (HDF5) containing the fragment ID, position in Earth-centered Earth-fixed (ECEF) coordinates, geographic coordinates, observation time, estimated altitude, and position uncertainty. As a metric of position uncertainty, we used the shortest distance between the two line-of-sight vectors from each camera. The estimated position uncertainties were 150 m and 480 m at the 67% and 95% percentiles, respectively.

One practical lesson learned for future optical observations is that accurate absolute timing is essential for fragment identification and triangulation during complex break-up events. The timing for the videos is provided by the network timing protocol, but the timing offset between the video frame timestamp and the time of exposure is not well known. Using a light emitting diode (LED) blinker synchronized to global positioning system (GPS) time, we determined that AllSky7 timing is at most 0.3 seconds offset from GPS time (Kastinen et al., 2025). One desirable modification to existing AllSky7 meteor cameras would be to incorporate an external optical timing reference, for example, with GPS-synchronized LED blinkers or similar timing fiducials visible in the camera frames, or alternatively, modifying the camera firmware to accept a time-stamping signal directly from a local GPS receiver or Network Time Protocol (NTP) server.

3.2 SIMONe Radar Measurements

In this work, we present the radar echoes detected with the following SIMONe Germany transmit-receive links: Juliusruh-Bornim, Juliusruh-Bornholm, Juliusruh-Hagenow, Juliusruh-Moitin, Kühlungsborn-Bornim, Kühlungsborn-Bornholm, Kühlungsborn-Hagenow, and Kühlungsborn-Moitin. Interferometric direction finding, together with transmit-receive delay measurements, provided estimates of the scattering location, received signal power, RCS, and Doppler shift.

Due to the rapid motion of the re-entry target, the echoes were processed using a range-Doppler matched filter bank at a 100 kHz Doppler bandwidth, with a 10 ms coherent integration window. This resulted in a $B_{rx} = 100$ Hz receiver noise bandwidth. This allowed for the detection of large Doppler shifts, typically associated with meteor head echoes. For details on the processing steps, refer to Chau et al. (2021), which discusses observations of fast-moving meteor head echoes using the

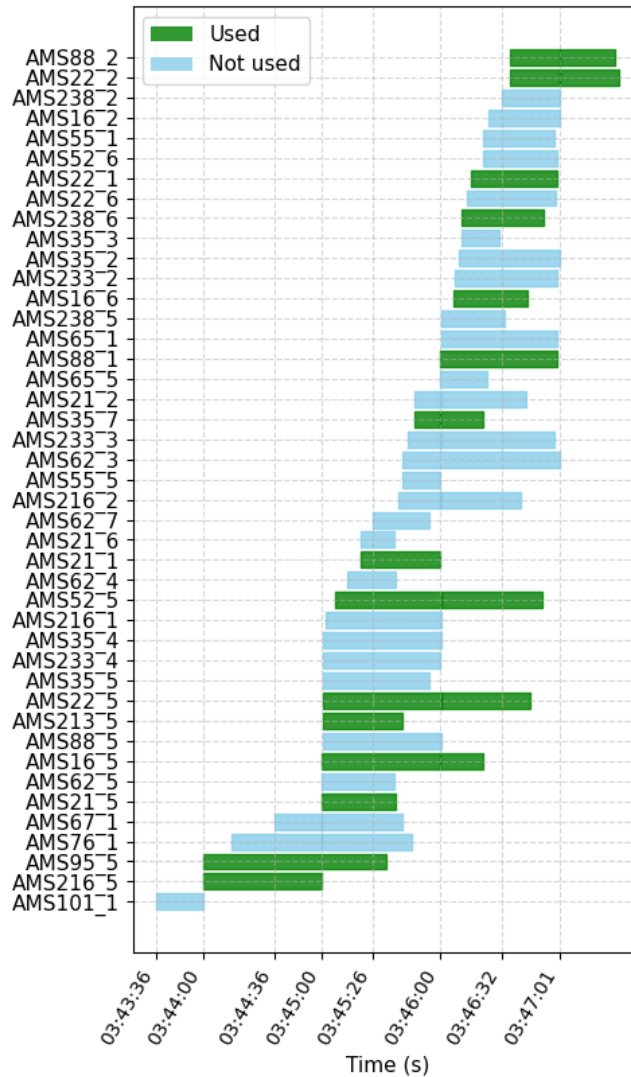


Figure 2. Visibility intervals of the fragments as seen from the available AllSky7 stations, where the underscored number indicate the per station camera id. This overview helped identify compatible observation pairs for triangulation and ensured coverage of all time segments.

same technique but with the SIMONE Peru system. Similar processing was also used to estimate the range and Doppler shift for a head echo associated with a fireball with SIMONE New Mexico (Obenberger et al., 2026).

Accurate Doppler shift, signal-to-noise ratio, and angle-of-departure (Chau and Clahsen, 2019) estimates were obtained using signals that are decoded with a compressive sensing approach based on Urco et al. (2019), which exploits the range sparsity of the observed echoes. The decoding consists of an iterative detection and removal of strong, medium, and weak echoes, followed by a final least squares inversion over all detected signals. We extended this approach to jointly handle

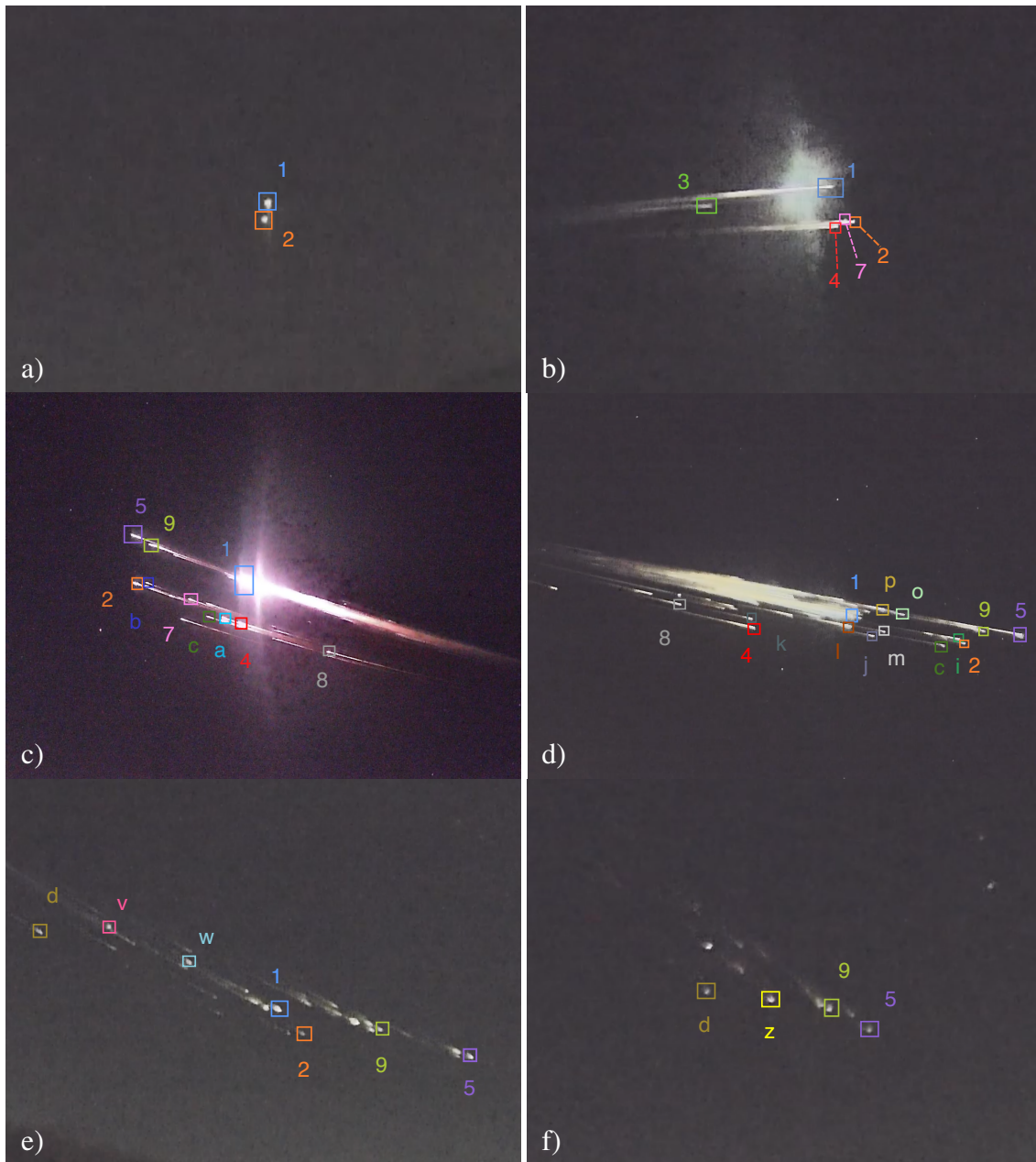


Figure 3. Six representative AllSky7 frames of the re-entry debris, ordered by time. Panels a–f show AMS95 at 03:44:30, AMS21 at 03:45:30, AMS35 at 03:46:02, AMS16 at 03:46:20, AMS88 at 03:47:00, and AMS22 at 03:47:15. Fragment identifiers for triangulated fragments are shown with colored numbers and letters. Panels c) and d) are during the time when radar echoes of the re-entry plasma were observed (3:46:00-3:46:30). All times are UTC.

multiple transmit sites within each iteration, where the detection is performed separately for each site before jointly subtracting all contributions from the measurements. This reduces the cross-interference between the two SIMONE Germany transmit sites in K uhlungsborn and Juliusruh, which transmit at the same frequency using pseudorandom codes.

The bistatic RCS was estimated from the measured signal-plus-noise to noise ratio,

$$\eta = \frac{S + N}{N}, \quad (1)$$

where η is expressed in linear units. Assuming receiver noise power

$$N = k_B T_{\text{noise}} B_{\text{rx}}, \quad (2)$$

the received signal power is

$$S = (\eta - 1)N. \quad (3)$$

The bistatic RCS is then estimated using

$$\sigma_b = \frac{S(4\pi)^3 R_{\text{tx}}^2 R_{\text{rx}}^2}{P_{\text{tx}} G_{\text{tx}} G_{\text{rx}} \lambda^2}, \quad (4)$$

where R_{tx} and R_{rx} are the transmitter-to-target and target-to-receiver ranges, P_{tx} is the transmit power, G_{tx} and G_{rx} are the transmit and receive antenna gains, and λ is the radar wavelength.

In the present analysis, the conversion was carried out with the fixed parameters used in the processing code: $f = 32.55$ MHz, $P_{\text{tx}} = 500$ W, $G_{\text{tx}} = G_{\text{rx}} = 1$, $B_{\text{rx}} = 100$ Hz, and $T_{\text{noise}} = 6000$ K. Although six transmitters were used, their contributions have been added incoherently. The estimated RCS values are based on a simplified radar equation, and they neglect additional effects such as polarization mismatch, detailed antenna pattern variations, and other propagation or processing losses. The values are not expected to be wrong by significantly more than a factor of 16.

3.3 Dynamic modeling of re-entry

For the ballistic trajectory fitting, we used a simple point-mass model in Earth-centered inertial (ECI) coordinates, i.e., fixed relative to the stars. Optical positions triangulated in ECEF coordinates were transformed to ECI coordinates. The fitted state obeys

$$\frac{d\mathbf{v}}{dt} = \mathbf{a}_g(\mathbf{r}) - \frac{1}{2} \rho_a(\mathbf{r}, t) B(t) \|\mathbf{v}_{\text{rel}}\| \mathbf{v}_{\text{rel}}, \quad (5)$$

where \mathbf{r} is the fragment position vector in ECI coordinates, \mathbf{a}_g is the gravitational acceleration including the Earth's J_2 term, and ρ_a is the atmospheric density evaluated using the NRLMSIS 2.1 model (Emmert et al., 2022). The drag is based on the velocity relative to the neutral atmosphere, $\mathbf{v}_{\text{rel}} = \mathbf{v} - \mathbf{v}_{\text{atm}}$, where \mathbf{v}_{atm} is the atmospheric velocity in the inertial frame. The factor $B(t)$ denotes the effective drag-to-mass parameter,

$$B(t) = \frac{C_D A \rho'_a}{m}, \quad (6)$$

where C_D is the drag coefficient, A is the effective cross-sectional area, ρ'_a is a relative correction to the atmospheric density accounting for the mismatch between the actual neutral density and the model density, and m is the fragment mass. All four of these terms in the ballistic coefficient are expected to vary during re-entry. To allow slow changes in drag behaviour during fragmentation, the ballistic coefficient was parameterized in log-space as $B(t) = 10^{\ell(t)}$, where $\ell(t)$ was linearly interpolated between four fitted node values over the observation interval.

The free parameters were therefore the initial ECI position \mathbf{r}_0 , initial ECI velocity \mathbf{v}_0 , and the four fitted node values defining $\ell(t)$. These parameters were estimated by minimizing the sum of squared position residuals,

$$S = \sum_{i=1}^N \|\mathbf{r}_{\text{mod}}(t_i) - \mathbf{r}_{\text{obs}}(t_i)\|^2, \quad (7)$$

using the triangulated optical positions $\mathbf{r}_{\text{obs}}(t_i)$. The initial guess was formed from the first triangulated position and a finite-difference velocity estimate from the first and last optical samples, and the model $\mathbf{r}_{\text{mod}}(t)$ was integrated numerically with a first-order Euler-Cromer (semi-implicit Euler) scheme using a fixed 0.5 s time step during the optimization.

The wind-corrected fits were carried out in two stages. First, a zero-horizontal-wind solution was obtained assuming atmospheric co-rotation, $\mathbf{v}_{\text{atm}} = \boldsymbol{\Omega}_{\oplus} \times \mathbf{r}$. ERA5 reanalysis winds (Hersbach et al., 2020, 2023) were then sampled along this nominal trajectory, converted to inertial atmospheric velocity $\mathbf{v}_{\text{atm}} = \boldsymbol{\Omega}_{\oplus} \times \mathbf{r} + \mathbf{v}_{\text{ERA5}}$, and interpolated in time for the final optimization. Above the highest altitude represented by the ERA5 profile, the horizontal wind was set to zero so that only atmospheric co-rotation contributed to \mathbf{v}_{atm} .

This simplified model can reproduce smoothly varying ballistic coefficients and velocities along the re-entry path, but it does not capture abrupt changes in ballistic coefficient associated with discrete fragmentation events. The results must therefore be treated with caution.

Because the drag model directly determines the ballistic coefficient, it also determines the specific kinetic-energy loss rate per unit mass. We therefore evaluated

$$\dot{\epsilon}_{\text{loss}} = -\mathbf{v}_{\text{rel}} \cdot \mathbf{a}_{\text{drag}} = \frac{1}{2} \rho_a(\mathbf{r}, t) B(t) \|\mathbf{v}_{\text{rel}}\|^3, \quad (8)$$

which provides a convenient diagnostic of where drag-related kinetic-energy dissipation is strongest without requiring an independent estimate of fragment mass or cross-sectional area. This quantity relies only on velocity and $B(t)$, and therefore allows relative comparisons of energy dissipation along the trajectory even when decoupled estimates of area, mass, and drag coefficient, and neutral density are unobtainable without additional assumptions.

To better understand the plasma production within the high temperature shock created by the hypervelocity entry giving rise to radar measurements, we also estimate the temperature T_{post} behind a steady normal shock. We use standard formula,

$$T_{\text{post}} = T_{\text{pre}} \frac{(2\gamma M_{\text{pre}}^2 - (\gamma - 1))((\gamma - 1)M_{\text{pre}}^2 + 2)}{(\gamma + 1)^2 M_{\text{pre}}^2} \quad (9)$$

that apply to adiabatic flows of a completely perfect fluid (Ames Research Staff, 1953; Anderson, 1989). Here T_{pre} is the atmospheric temperature, M_{pre} is the Mach number of the flow before the shock, and γ is the specific heat ratio of the gas.

The above equation can be derived from the Rankine-Hugoniot relations, and the estimated post-shock temperature should be treated as a diagnostic of the possibility for the shock to produce enough free electrons to allow radio wave scattering.

4 Results

4.1 Optical fragment trajectories

Figure 4a shows the altitude of the fragments detected with the meteor cameras as a function of time. At the time when the first triangulations were possible, one fragment F_1 was visible at an altitude of 85.3 km at 3:44:00 UTC. A second fragment F_2 appeared at an altitude of 78.5 km at 3:44:15. These two fragments continued to fragment further, with the most intense fragmentation occurring at an altitude of 60 km. Fragments associated with F_2 crossed 60 km at approximately 3:45:51, whereas the higher altitude fragment F_1 crossed 60 km at approximately 3:46:22. The last triangulated fragment was observed at an altitude of 40 km at 3:47:25. The lowest triangulation was made for a fragment associated with F_2 at an altitude of 36 km at 3:47:12.

4.2 Ballistic fits and specific energy loss

Panels b) and d) of Figure 4 show a representative subset of ballistic fits overlaid on all triangulated optical fragment positions. Not all possible chains of fragmentation were fit, but the subset shown captures the main behavior of both fragment families and provides a compact illustration of the inferred dynamical evolution. Panel b) shows that the fitted speeds relative to the atmosphere start at 7 km s^{-1} and are around 3 km s^{-1} when optical fragments disappear. Panel d) shows that the fitted specific kinetic-energy loss rate per unit mass is highest over a broad altitude range from roughly 30 to 60 km.

The estimates shown in Figure 4b,d are most reliable within the altitude interval constrained by the optical measurements and are expected to be most robust near the middle of that interval, around 60 km altitude. Above and below the observed range, the trajectories, relative speeds, and energy-loss rates rely increasingly on extrapolation and should therefore be interpreted with caution.

The extrapolation of the fit for the fragment chain (F_2, F_7, F_a, F_k) shown in Figure 4b,d reaches the ground near the longitude of one of the recovered debris fragments. Figure 5 shows the fit for this fragment chain in more detail, including the fitted ballistic coefficient and the spread of trajectories obtained from the linearized parameter uncertainty. However, the extrapolated impact locations should not be interpreted as precise predictions. The ballistic coefficient changes substantially over the course of fragmentation, and this evolution is difficult to model and fit robustly with the present parameterization. Therefore, the estimated parameters carry a significantly larger uncertainty than the linearized uncertainties would indicate.

A summary of the fitted ballistic coefficients, peak dynamic quantities, and ECEF speeds at selected altitude levels is given in Table 1. The quoted 2σ uncertainties are derived from the fitted parameter covariance and propagated to the reported quantities. These values are most informative within the altitude interval constrained by the optical measurements.

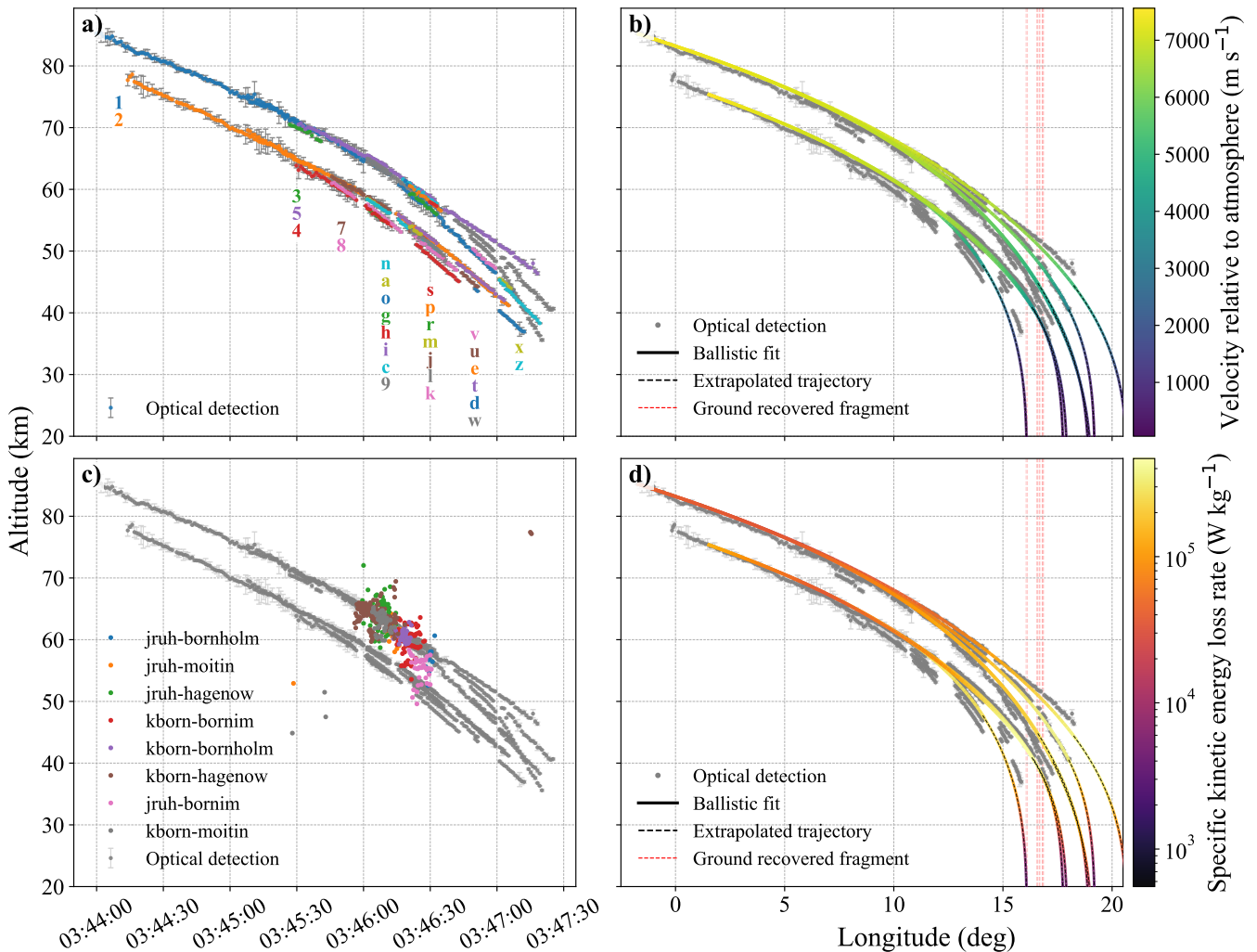


Figure 4. Overview of the optical, dynamical, and radar results in time–altitude and longitude–altitude coordinates. Panel a) shows the triangulated optical fragment detections with the fragment identifier as a function of time and height. Panel b) shows a representative subset of ballistic fits colored by velocity relative to the atmosphere (longitude vs height). Panel c) shows the positions of optical fragment and radar detections of the re-entry plasma (time vs height). Panel d) shows specific kinetic energy loss per unit mass (longitude vs height). Red vertical lines indicate longitudes of ground recovered fragments.

4.3 RCS and Doppler signatures

Figure 6 shows the corresponding $(S+N)/N$ measurements for all eight radar links that detected the event. The radar signature associated with the re-entry plasma appears as a parabolic arc, first approaching in range, then reaching maximum power near the closest point corresponding to specular geometry, and finally receding. The observed range interval and temporal evolution of this radar echo differ between links due to variations in transmitter–receiver geometry relative to the re-entry trajectory. In

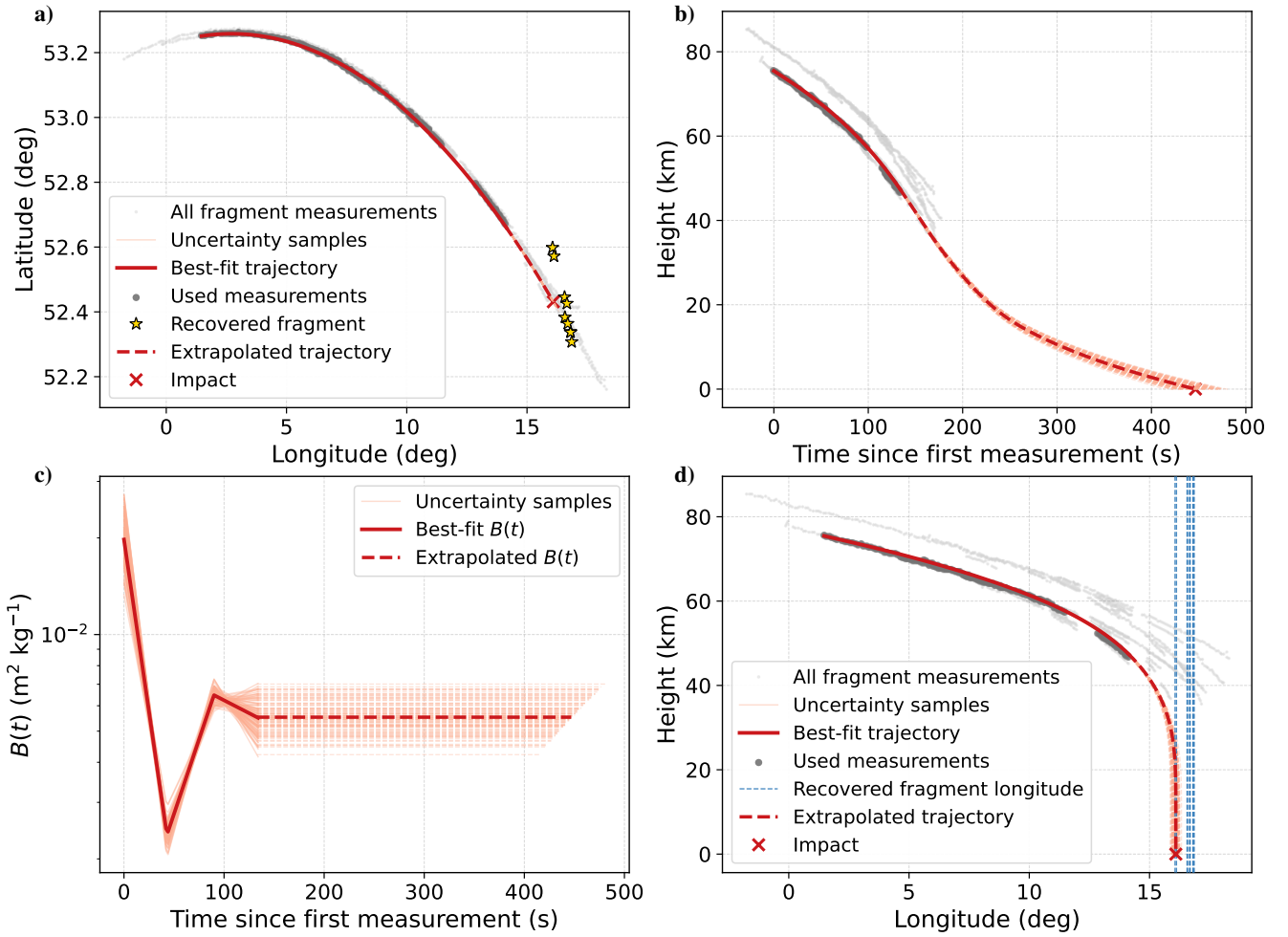


Figure 5. Example ballistic fit for the fragment chain F_2, F_7, F_a, F_k . Gray markers show all triangulated optical positions, darker gray markers show the measurements used in this fit, the solid red curve is the best-fit trajectory, the light red curves show 100 uncertainty samples, and the dashed red curve shows the extrapolated trajectory toward the nominal impact point. Panel a) shows the latitude-longitude ground projection, panel b) altitude versus time, panel c) the fitted ballistic coefficient, and panel d) longitude versus altitude, together with the recovered fragment locations.

panel h), the open circles show the bistatic propagation ranges expected from the triangulated optical fragment positions after shifting the optical times later by 1.5 s. White circles denote fragments associated with the F_1 family, and red circles denote fragments associated with the F_2 family. Both fragment families align with the range-time locations of the non-specular radar echoes in this link.

Figure 7a) shows the estimated RCS measured using the Kühlungsborn-Hagenow link as a function of time and bi-static propagation range (the sum of the distance from the transmitter to the target and from the target to the receiver). The predicted

Table 1. Summary of the fitted fragment chains. B_0 and B_1 denote the fitted start and end ballistic coefficients in units of $10^{-3} \text{ m}^2 \text{ kg}^{-1}$. The diameter column gives a rough effective spherical-equivalent size range inferred from B_0 and B_1 assuming $C_D = 2$, an initial bulk density of 30 kg m^{-3} , and a terminal bulk density of 1000 kg m^{-3} . Peak dynamic pressure and peak specific energy-loss rate are reported; uncertainties are estimated as approximate 2σ spreads from 50 covariance-drawn trajectory samples. The speed entries give the absolute ECEF speeds at the downward crossings of 70 and 40 km altitude; their uncertainties are estimated as 2σ spreads from 50 covariance-drawn trajectory samples.

Path	B_0	B_1	$d_0 \rightarrow d_1$	q_{\max}	$\dot{e}_{\text{loss},\max}$	$ \mathbf{v} _{70}$	$ \mathbf{v} _{40}$
Units	$10^{-3} \text{ m}^2 \text{ kg}^{-1}$	$10^{-3} \text{ m}^2 \text{ kg}^{-1}$	m	kPa	kW kg^{-1}	km s^{-1}	km s^{-1}
F_1	31.6 ± 9.9	2.6 ± 0.4	$3.16 \rightarrow 1.17$	33.3 ± 5.3	294.9 ± 3.9	6.90 ± 0.01	3.93 ± 0.19
F_2	24.1 ± 9.1	3.7 ± 0.7	$4.14 \rightarrow 0.81$	26.3 ± 2.0	373.9 ± 26.4	7.14 ± 0.02	3.74 ± 0.16
F_1, F_5	31.6 ± 9.9	2.8 ± 0.2	$3.16 \rightarrow 1.08$	32.4 ± 2.1	368.2 ± 13.6	7.10 ± 0.01	4.04 ± 0.10
F_1, F_9	31.6 ± 9.9	5.2 ± 0.6	$3.16 \rightarrow 0.58$	20.2 ± 1.2	373.0 ± 13.7	7.00 ± 0.01	3.18 ± 0.13
F_2, F_7, F_a, F_k	24.1 ± 9.1	5.6 ± 1.5	$4.14 \rightarrow 0.54$	12.5 ± 2.5	276.5 ± 20.2	7.14 ± 0.02	2.59 ± 0.30
F_2, F_7, F_i, F_t	24.1 ± 9.1	4.9 ± 1.0	$4.14 \rightarrow 0.61$	26.4 ± 1.5	462.1 ± 33.8	7.12 ± 0.02	3.59 ± 0.21
F_1, F_p, F_w, F_z	31.6 ± 9.9	1.8 ± 0.3	$3.16 \rightarrow 1.65$	44.3 ± 6.4	270.7 ± 5.4	6.91 ± 0.01	4.10 ± 0.11

full propagation range based on the fitted trajectory of fragment F_1 is shown with a white dashed line, which appears to be shifted by 1-2 seconds earlier than the similar parabolic arc painted by the radar echoes.

The top axis of Figure 7a) shows the aspect angle based on the fitted trajectory of fragment F_1 :

$$\theta = \arccos\left(\frac{\mathbf{k}_B \cdot \mathbf{v}}{\|\mathbf{k}_B\| \|\mathbf{v}\|}\right) \quad (10)$$

where \mathbf{k}_B is the bi-static Bragg wave vector and \mathbf{v} is the velocity vector of the scattering re-entry fragment. The peak RCS is observed near the specular aspect angle (90°). There are also several other localized enhancements in RCS, which might be associated with other fragments passing through the specular aspect angle at different times.

Figure 7b) shows the Doppler shift based on the range-Doppler matched filter bank for the Kühlungsborn-Hagenow link. The colors in the plot are restricted to ± 100 Hz because no larger values were estimated. Note that the minimum and maximum values in the pass band of the analysis are ± 50 kHz. Figure 7c) shows the expected Doppler shift for this radar link based on the motion of fragments F_1 and F_2 with the assumption that the scattering plasma moves at the same velocity as the parent fragment, as would be the case with a meteor head echo (Close et al., 2007).

To illustrate the temporal evolution of the strongest echo in more detail, Figure 8 shows the estimated RCS for the Kühlungsborn-Hagenow link at the range gate with the highest echo power. The time series was evaluated at a time resolution of 10 ms and converted to RCS using a 100 Hz noise bandwidth together with the transmitter-to-target and target-to-receiver ranges inferred from the trajectory of fragment F_1 . The peak RCS is 61.5 dBsm, with the noise equivalent RCS around 15 dBsm. An exponential decay fit applied over the interval 03:46:05–03:46:07 UTC gives an e-folding time of 0.69 ± 0.13 s (2σ), indicating that

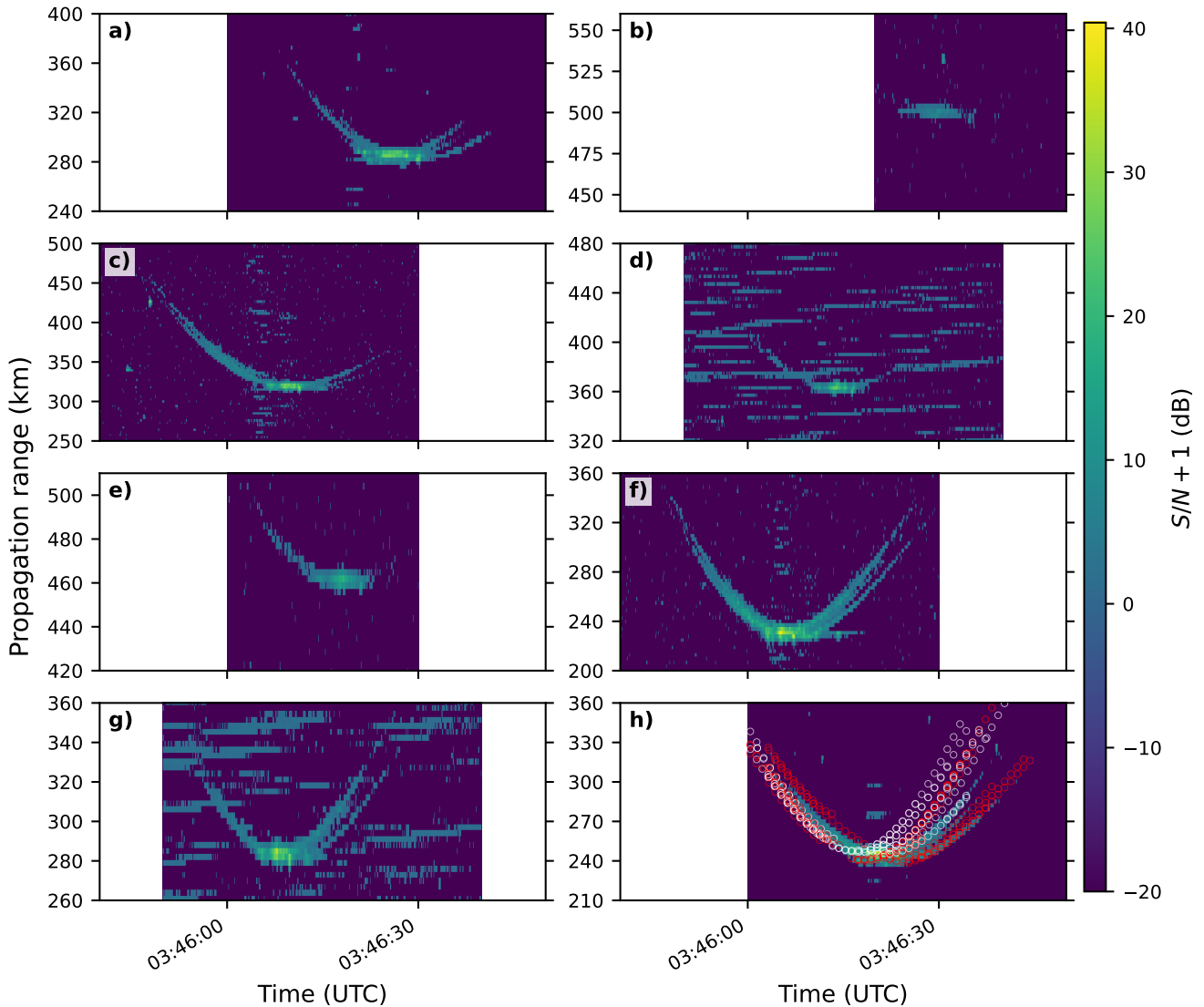


Figure 6. $(S + N)/N$ in dB with 100 Hz noise bandwidth as a function of time and propagation range for the eight SIMONE transmitter-receiver links that detected the event. Each panel shows one bistatic link with a panel-specific propagation-range interval chosen to show the echo region. Optical fragment positions are overlaid only in panel h): open circles show the propagation ranges computed from triangulated optical positions after shifting the optical times later by 1.5 s. White circles indicate the F_1 fragment family, and red circles indicate the F_2 fragment family. Both families coincide with the non-specular radar echo ranges in this panel.

the strongest scattering structure decays on a sub-second timescale. There are three local maxima in the RCS that are likely to coincide with plasma irregularities from three different nearby fragments passing through the specular point in the radar geometry.

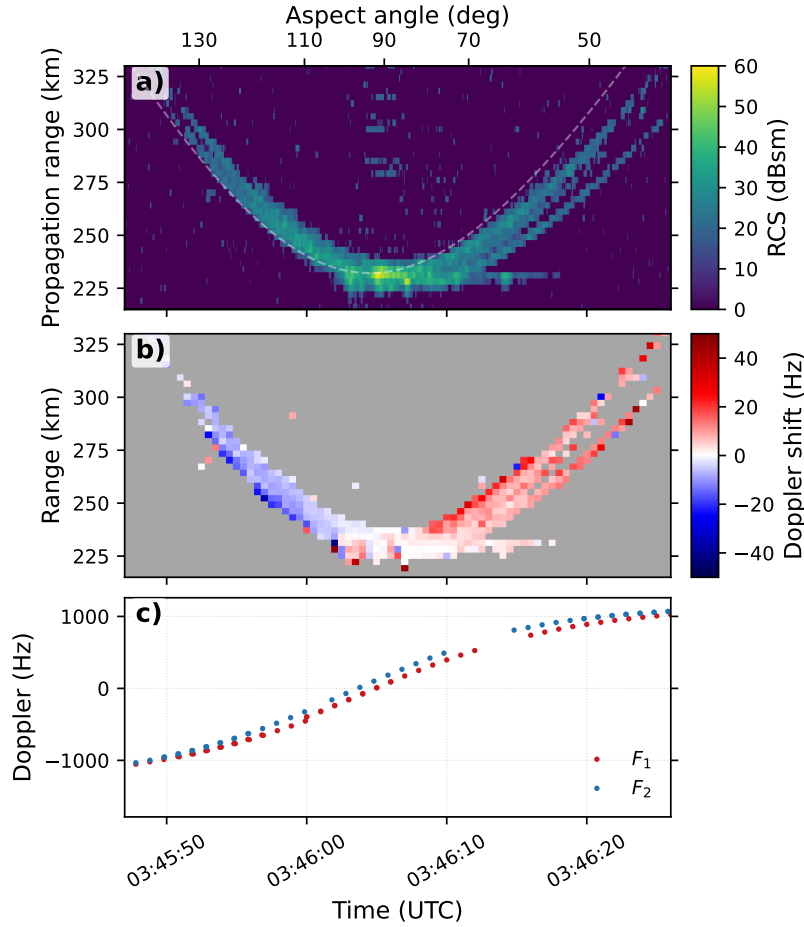


Figure 7. Radar signatures for the Kühlungsborn-Hagenow link. Panel a) shows the estimated RCS as a function of time and propagation range. Panel b) shows the Doppler shift. Panel c) shows the Doppler shift predicted from the fitted trajectories of fragments F_1 and F_2 .

4.4 Radar detections relative to the optical fragments

Panel c) of Figure 4 shows the radar detections together with the optical fragment trajectories. The radar echoes are observed at altitudes between 55 km and 70 km and primarily overlap with fragment F_1 and its child fragments. However, the Juliusruh-Bornim link detects echoes that align better with fragment F_2 . The clustering of detections is consistent with the enhancement of RCS near the specular aspect angle, where the fragment velocity vector is perpendicular to the Bragg wave vector of the transmit-receive path. Different radar links satisfy this specular condition at different positions along the re-entry path. Scatter with non-specular aspect angles is also detected with all links, but this scatter always has a lower signal-to-noise ratio than the specular aspect echoes. For noisier links, the non-specular echoes are less discernible but visible on all links, with the exception of Bornholm.

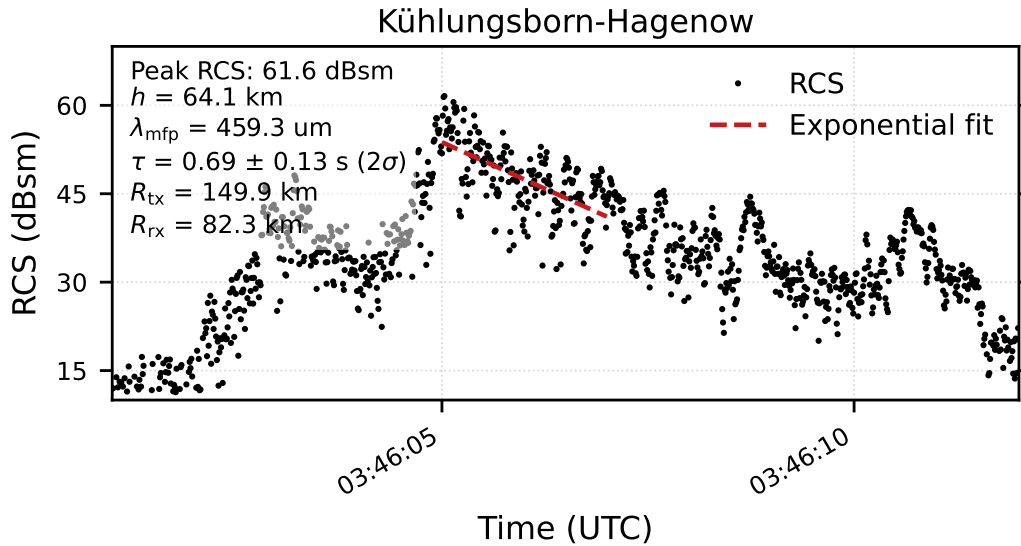


Figure 8. Estimated RCS as a function of time for the Kühlungsborn-Hagenow range gate with the highest $(S+N)/N$. The conversion from measured power to RCS uses the transmitter-to-target and target-to-receiver ranges estimated from the fitted trajectory of fragment F_1 . The dashed line shows an exponential fit over the interval 03:46:05–03:46:07 UTC.

Figure 9 summarizes the altitude distribution of fragment detections in the optical data together with the altitude distribution of radar detections. Panel a) shows a histogram of the altitudes of all fragments detected in cameras. The distribution indicates that fragment creation was most active between about 40 and 65 km altitude. The histogram also shows the distribution of altitudes of radar detections localized with radar range and angle of departure. Radar detections are found between 50 and 70 km altitudes. The dashed Gaussian fit to the optical detection heights has a maximum at 60 km with a standard deviation of 10 km, quantifying the broad altitude band over which the optical fragmentation is concentrated. Panels b)–d) show derived quantities obtained from the ballistic fits: specific kinetic-energy loss rate per unit mass, velocity, and estimated post-shock temperature. The gray bands in panel d) mark the Knudsen number thresholds characterizing the continuum-flow regime for a 1 m object, assuming the trajectory of fragment F_1 . Thresholds of $\text{Kn} < 0.01$, $\text{Kn} < 0.001$, and $\text{Kn} < 0.0001$ are shown. The dashed lines indicate the portions of the fits that extrapolate outside the range of measurement points. The values of the derived parameters are expected to be of lower quality at the edges of the measurement interval and within the extrapolation portion of the fit.

5 Discussion

The triangulated optical positions shown in Figure 4a show that there are two fragment families. Child fragments of fragment F_1 ($F_3, F_5, F_9, F_n, F_o, F_p, F_r, F_s, F_w, F_v, F_x$, and F_z), and F_2 ($F_4, F_7, F_8, F_a, F_c, F_h, F_g, F_i, F_m, F_j, F_\ell, F_k, F_t, F_u$,

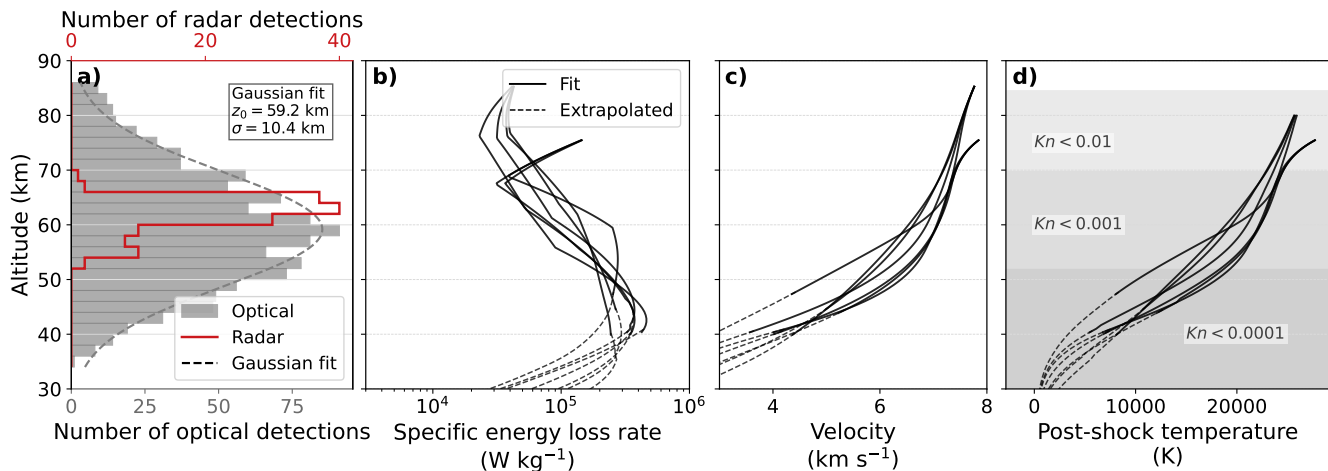


Figure 9. Summary of the altitude distribution and fitted dynamical evolution of the re-entry fragments. Panel a) shows the altitude histogram of all optical fragment detections from the triangulations together with the altitude histogram of radar detection heights from SIMONE. In panel a), the dashed Gaussian fit to the optical distribution indicates a broad maximum centered at 60 km with a standard deviation of 10 km, showing that most optical detections cluster in the same altitude region where the radar detections are concentrated. Panel b) shows the fitted specific energy loss rate as a function of altitude for the ballistic fits, with dashed segments indicating extrapolated trajectories below the observed range. Panel c) shows the corresponding fitted fragment speeds. Panel d) shows the corresponding estimated post-shock temperatures; the gray altitude bands mark the continuum-flow regions for 1 m objects, using Knudsen number thresholds of 0.01, 0.001, and 0.0001.

F_e , and F_d). It is not possible to determine from the measurements a point where F_1 and F_2 are separated, as this has occurred above 85 km altitude, where the first observation is made.

The red dashed vertical lines in panels b) and d) of Figure 4 show the longitudes of the ground-recovered fragments in Poland reported by Kruzynski et al. (2025). Based on the fitted trajectories, the lower fragment F_2 and its child fragments are the most likely candidates for the recovered debris, because many fragments associated with the upper fragment F_1 continue further down range than the recovery locations. According to (Kruzynski et al., 2025), the recovered debris consists of carbon fiber propellant tank parts and thin metallic sheets. These components have relatively high area-to-mass ratios, which is consistent with the fragments of the F_2 family decaying faster than fragments of the F_1 family, as seen in Figure 9c. None of the recovered fragments were associated with the Merlin Vacuum (MVac) engine, which is expected to be more heat-tolerant and to have a lower area-to-mass ratio than the second-stage tank structure. This supports the interpretation that fragment F_2 is associated with the second-stage tank structure and fragment F_1 is the MVac engine.

The diameter estimates listed in Table 1 should be interpreted with substantial caution. They were derived by converting the fitted ballistic coefficients into spherical-equivalent diameters using $B = C_D A/m$, which corresponds to assuming $\rho'_a = 1$ in the dynamic model, together with an assumed drag coefficient of 2, an initial bulk density of 30 kg m^{-3} motivated by published Falcon 9 upper-stage dimensions and mass (Space Exploration Technologies Corp., 2025), and a terminal bulk density of

1000 kg m^{-3} intended to represent denser compact fragments after breakup. In reality, the fragments are not spherical, their drag coefficients are unknown and likely vary with attitude and flow regime, the bulk density can change by orders of magnitude as cavernous structures fragment into smaller pieces, and ρ'_a can vary 10-40% due to various atmospheric waves (Fritts and Alexander, 2003; Huyghebaert et al., 2025). In addition, the fitted time variable ballistic coefficient is itself only an effective parameterization of a complex fragmentation process. The resulting diameter estimates are therefore at best order-of-magnitude indicators rather than precise size determinations.

The characteristics of the range-migrating radar echoes shown in Figure 7 differ from those of meteor head echoes. Although the radar detections approximately track the optical fragments in range and position, the measured Doppler shifts in Figure 7b) are much smaller than expected from the fragment motion shown in Figure 7c) (tens of Hz instead of up to ± 1000 Hz). This implies that the scattering plasma is not moving at the same velocity as the object producing it, as would be expected for a meteor head echo that originates from the plasma surrounding the ablating object. In this observation, the Doppler shift indicates motion close to the atmospheric velocity (< 100 m/s). A small fraction of the re-entry object's motion may still be retained, as a slight motion along the trajectory is detectable in the Doppler shift.

The direct optical range overlay in panel h) of Figure 6 shows that the triangulated F_1 and F_2 fragment families coincide with the ranges of the non-specular radar echoes after shifting the optical fragment times later by 1.5 s. This shift is consistent with the observed radar echo trailing the optical fragment trajectory by about 1–2 seconds. This indicates that the radar echo originates from turbulent plasma in the wake of the re-entry debris. Such turbulence would take some time to develop (Oppenheim et al., 2003) before significant scattering at non-specular aspect angles can appear. The fact that the non-specular echo appears to track the motion of the fragments without significant time or range extent suggests that this wake plasma also decays rapidly. This decay time is approximately one second, based on the e-folding time fit to the specular portion of the radar echo shown in Figure 8. The turbulent wake plasma interpretation is broadly consistent with earlier suggestions from the Mercury capsule and Ariane 5 EPC studies Lin (1962); Rubin et al. (2005). Lin also found that the brightest radar return lagged the capsule by at least 0.6 s, corresponding to about 4.2 km, which is consistent with our observation.

The re-entry vehicle produces a plasma sheath, which surrounds the re-entry fragments. This is evident from the loss of radio communications for re-entering spacecraft (Kim et al., 2008). However, we do not observe a meteor head echo-like echo from the plasma surrounding the ablating spacecraft, despite the use of a range-Doppler matched filter that permitted large Doppler shifts. The likely reason is the width of the plasma sheath surrounding the spacecraft. It is expected to be not much larger than the re-entry fragment, as the mean free path at 60 km is only around 1 mm. Thus, the RCS of the head echo is not expected to be much larger than the size of the parent fragment that produces the plasma sheath surrounding the spacecraft. The Falcon 9 second stage is approximately 15 m long and 3.66 m in diameter, excluding the payload adapter and fairing (Space Exploration Technologies Corp., 2025). Even taking the circular cross section of a 3.66 m diameter stage as a crude geometric upper bound gives only about 10 m^2 , which is still well below the 100 m^2 detection limit of the SIMONE radar system for the location where the radar echoes were detected. However, once the plasma turbulence within the wake develops sufficiently, the RCS is increased above the detection limit. Had the re-entry debris been tracked with a more powerful radar, such as an MST radar,

it is likely that the objects could have been tracked using direct scatter from the fragments themselves, without a significant increase in RCS due to the plasma sheath.

While the optical data does not allow absolute intensity of optical emissions to be estimated, visually the main fragment F_1 is significantly brighter than fragment F_2 , as shown in Figure 3. This indicates higher temperature and hence higher plasma production. This is consistent with radar signatures primarily being associated with fragment F_1 , as shown in Figure 4. As discussed earlier, this fragment is suspected to be associated with the MVac engine, which implies that the composition and the ballistic coefficient of the re-entry object could play an important role in the radar detectability of re-entry debris with radar.

The enhancement of RCS at specular geometry, shown in Figure 7a) together with the small observed Doppler shifts in Figure 7b), has a resemblance with overdense specular meteor trail echoes (McKinley, 1961; Poulter and Baggaley, 1977). Such an enhancement was also reported by Lin (1962) and Rubin et al. (2005). This enhancement at specular aspect angle suggests that there is a narrow, elongated plasma structure within the 1-2 km long Fresnel zone along the path of the re-entry debris, which contributes coherently to the formation of a radar echo, with a cross-track extent less than the radar wavelength of 9.2 meters. The echo power decay time constant of 0.7 ± 0.1 s is significantly shorter than typical e-folding timescales of overdense specular meteor trails. One explanation is that D-region recombination ion chemistry is the main controlling factor for trail decay in the 55-65 km altitude range, instead of the much slower ambipolar diffusion, which becomes more effective than ion chemistry at higher altitudes (Turunen, 1996; Younger et al., 2014). It is expected that the chemical composition of the ablated material will also influence the ion chemistry.

The production of plasma around re-entering orbital objects differs from that of meteors. The re-entry debris observed in this study has velocities of $6-7 \text{ km s}^{-1}$ at the time when radar echoes are observed, as shown in Figure 9. Meteor head echoes are rarely detected at such low velocities because they fall below the impact-ionization threshold that governs plasma formation for faster meteoroids (Vondrak et al., 2008). This implies that atoms ablated from the heated spacecraft would not ionize efficiently through collisions with atmospheric molecules alone. However, strong plasma echoes were still detected with very large RCS values. The ionization mechanism for the observed plasma is the high temperature shock front. At around 60 km altitude, the Knudsen number, which is the ratio of the mean free path to the object scale size $\text{Kn} = \lambda_{\text{MFP}}/L$ is rather low. Based on Table 1, the fragments detected optically with the cameras are estimated to have diameters in the 0.5-5 meter range with Knudsen numbers $0.0002 < \text{Kn} < 0.002$ in the continuum flow regime, which is a necessary condition for a ionizing high temperature shock front to form (Grossir et al., 2018; Esposito et al., 2024). Figure 9d illustrates the estimated post-shock gas temperature using Equation 9. Limiting estimations to $\text{Kn} < 0.005$, the temperatures indicate that significant plasma production can occur due to the shock above 40 km. Even though it is outside the scope of this study to simulate the shock plasma production precisely, typical relations such as the Saha ionization equation, show that significant thermal ionization begins at 10-20 kK (He et al., 2021).

The mean free path at 60 km is around 1 mm, so objects larger than 1 cm could potentially produce an ionizing shock front at this altitude (Grossir et al., 2018). Applying equation 5 to modeling of orbital circular orbit re-entry indicates that objects smaller than 1 cm would decelerate significantly due to atmospheric drag before reaching an altitude where the slip-flow or continuum-flow regime necessary for plasma formation exists. Thus, objects smaller than this are unlikely to create

sufficient plasma density to allow detection by specular meteor radars. The fact that we only see signatures of four fragments in the specular and non-specular radar echoes, indicates that there is a lower size threshold for sufficient plasma production to be detectable by specular meteor radar systems, and this threshold for the SIMONe radar system is around 1 meter based on the number of fragments detected with the radar, the diameters estimated based on the ballistic fits, and the size of the Falcon second stage. More detailed modeling of the plasma production and radar scattering would be needed to determine the expected radar signatures for different fragment sizes and to constrain the size threshold for radar detectability with different radar systems.

Understanding the differences between the re-entry behaviour of meteors and the slower, uncontrolled re-entry of the Falcon 9 is essential for quantifying the impact of space debris re-entry on the middle atmosphere. As noted in the introduction, Wing et al. (2026) observed a lithium plume which formed as the Falcon 9 hull heated above 933 K upon re-entry at an altitude near 100 km. In that study, the authors used a simplified model for the ablation of aluminium rockets, which neglected rocket body fragmentation, shock-front formation and ionisation. The authors of the study also acknowledged in their discussion that the re-entry trajectory of the Falcon 9, provided by ESA, was the largest source of uncertainty in linking the detection of a mesospheric lithium plume to the Falcon 9. The use of camera and radar networks to accurately characterise the re-entry trajectory, including plasma generation of debris fragments, would address the weakest aspect of that study and could provide a strong contribution for future studies of its kind and potential environmental monitoring activities. The Gaussian fit to the optical detection-height distribution in Figure 9a, centered at 60 km with $\sigma = 10$ km, provides an observational summary of where fragmentation was most visible. While this is not a direct measurement of mass deposition, the distribution of optical signatures is expected to be correlated with it and therefore offers a useful empirical constraint for comparisons with the altitude range of material deposition discussed by Murphy et al. (2023).

6 Conclusions

This study provides a dataset of 30 fragment trajectories derived from stereoscopic triangulation of the February 19th 2025 Falcon 9 upper-stage re-entry. During the most intense phase of the breakup, between 55 km and 70 km altitude, not every visible fragment could be identified because of the large number of simultaneously visible objects. Nevertheless, the reconstructed trajectories show that the lower fragment family F_2 is likely the propellant tank assembly and the source of the recovered ground debris, whereas the upper fragment family F_1 is consistent with a denser MVac engine. Ground recovered fragments were associated with fragments that broke off of F_2 , whereas radar signatures were linked primarily to the optically brighter fragment F_1 .

The dynamic fit of the trajectories indicates that the largest kinetic-energy loss occurs at 30–70 km altitude, which is also where the largest number of optical fragments and the radar echoes were observed. Modeling and ablation chemistry studies suggest that re-entering space materials deposit material into this altitude range (Murphy et al., 2023), which agrees with the observations. Without additional re-entry modeling that uses a more detailed engineering model, such as SCARAB (Lips et al., 2004), it is not possible to determine precisely how the mass deposition is distributed with altitude. Comparing the

observations in this study with such a model would therefore be an valuable next step. It is possible that the radar echoes can help constrain such models, because they provide independent information on the altitude range where plasma production and mass loss occur. The optical observations, even though not absolutely calibrated, could also yield useful constraints on radiation losses during re-entry, allowing better constraints on heating rates of the spacecraft. Further, co-location with lidars would allow for additional constraints by simultaneously evaluating the re-entry trajectory, geophysical dynamics as well as composition for both mesospheric metals produced during ablation as well as potential stratospheric aerosols which may be produced during fragmentation. The fitted optical altitude distribution, with a peak at 60 km and a standard deviation of 10 km, provides a compact observational benchmark for that comparison. Although it is not a direct measurement of mass deposition, the optical-signature distribution is expected to be correlated with the altitude range where deposition is strongest.

Two distinct types of radar echoes were observed: 1) radar echoes at non-specular aspect angles with 30-40 dBsm RCS, 2) echoes with enhanced RCS at specular aspect angles, with up to 60 dBsm RCS. The suggested mechanism of ionization is a superheated plasma created within the hypervelocity shock front. The non-specular aspect angle echoes are explained as ionized wake turbulence, and the specular echoes are explained as a structure similar to overdense specular meteor trail echoes (McKinley, 1961; Poulter and Baggaley, 1977).

As shown in this study, fairly low power all sky meteor radar systems are able to observe re-entry plasma with significant RCS enhancements due to plasma produced. These echoes are likely to be observed in the region where slip flow or continuum flow conditions are met, which is expected to be below 60 km altitude for objects larger than a few centimeters in size. There are many similar systems around the world, each with a collecting area in the order of 100000 km². These systems could potentially contribute in the future to monitoring the re-entry of space debris. It is possible that more sensitive radars could detect plasma trails of smaller re-entry objects than shown in this study, which are expected to produce ionization when they are in the continuum flow regime.

In this study, the fragments that produced radar echoes are estimated to be in the 0.5–5 m size range. Objects of this size are already tracked by the U.S. Space Surveillance Network, so radar observations are not expected to provide substantial additional information about the number of re-entering objects. However, meteor radar and optical observations can provide useful information about plasma production and mass deposition during re-entry, which is important both for understanding the impact of space-debris re-entry on the atmosphere and for improving ground-impact hazard assessment.

Data availability. The optical and radar dataset associated with this study is publicly available (Vierinen, 2026b). ERA5 pressure-level reanalysis data used for the wind correction were obtained from the Copernicus Climate Change Service Climate Data Store (Hersbach et al., 2023).

Author contributions. JV led the analysis and manuscript preparation. DKn contributed optical data analysis. JLC, GB, DH, MC, NP, TR, RW, and KSO contributed radar observations, analysis, and interpretation. BG contributed optical calibration and interpretation. DKa contributed interpretations of the re-entry. All authors contributed to discussion of the results and manuscript revision.

Competing interests. The authors declare that they have no conflict of interest.

Acknowledgements. Part of the work presented here is based on data from the AllSky7 camera network (allsky7.net). We thank the camera operators of the AllSky7 network for providing optical observations used in this study: John Downing (AMS101), Jörg Strunk (AMS21), Sebastian Schmidt and Johannes Schultz (AMS216), Jochen Schönfelder (AMS233), Sirko Molau (AMS35), Gerhard Lehmann (AMS55), Martin Fiedler (AMS65), Bernd Klemt (AMS76), Björn Poppe and Theresa Ott (AMS95), Sirko Molau (AMS16), Julia Lanz-Kröcher (AMS213), André Knöfel (AMS22), Stiftung Planetarium Berlin (AMS238), Peter Kroll, Mario Ennes, and Thomas Müller (AMS52), Maciej Libert and Jan-Gerd Mess (AMS62), Luc Bastiaens (AMS67), and Peter Lindner (AMS88). This work contains modified Copernicus Climate Change Service information (2025). Neither the European Commission nor ECMWF is responsible for any use that may be made of the Copernicus information or data it contains. Large language models were used for grammar and programming assistance only. JLC and MC acknowledge support from the European Office of AFOSR 717 (EOARD) grant FA8655-23-1-7017.

References

- Ames Research Staff: Equations, Tables, and Charts for Compressible Flow, Tech. Rep. NACA-TR-1135, National Advisory Committee for Aeronautics, Washington, D.C., 1953.
- Anderson, J. D.: Hypersonic and high temperature gas dynamics, AIAA, 1989.
- Bartková, D., Šilha, J., Tóth, J., Kornoš, L., Lemmens, S., and Jilete, B.: Investigation of the CZ-3B R/B Third Stage Fragmentation during Re-Entry, in: 2nd International Orbital Debris Conference, vol. 2852, p. 6037, 2023.
- Chau, J. L. and Clahsen, M.: Empirical Phase Calibration for Multistatic Specular Meteor Radars Using a Beamforming Approach, *Radio Science*, 54, 60–71, <https://doi.org/10.1029/2018RS006741>, 2019.
- Chau, J. L., Urco, J. M., Vierinen, J. P., Volz, R. A., Clahsen, M., Pfeffer, N., and Trautner, J.: Novel specular meteor radar systems using coherent MIMO techniques to study the mesosphere and lower thermosphere, *Atmospheric Measurement Techniques*, 12, 2113–2127, <https://doi.org/10.5194/amt-12-2113-2019>, 2019.
- Chau, J. L., Urco, J. M., Vierinen, J., Harding, B. J., Clahsen, M., Pfeffer, N., Kuyeng, K., Milla, M., and Erickson, P. J.: Multi-static specular meteor radar network in Peru: System description and initial results, *Earth and Space Science*, 8, e2020EA001293, <https://doi.org/10.1029/2020EA001293>, 2021.
- Chau, J. L., Urco, J. M., Weber, T., and Aweda, J. O.: Atmospheric Radar Imaging Improvements Using Compressed Sensing and MIMO, pp. 369–400, Springer International Publishing, Cham, ISBN 978-3-031-09745-4, https://doi.org/10.1007/978-3-031-09745-4_12, 2022.
- Close, S., Brown, P., Campbell-Brown, M., Oppenheim, M., and Colestock, P.: Meteor head echo radar data: Mass–velocity selection effects, *Icarus*, 186, 547–556, <https://doi.org/10.1016/j.icarus.2006.09.007>, 2007.
- Cong, Z., Chen, R., and He, Z.: Numerical modeling of EM scattering from plasma sheath: A review, *Engineering Analysis with Boundary Elements*, 135, 73–92, <https://doi.org/10.1016/j.enganabound.2021.11.013>, 2022.
- Emmert, J. T., Jones Jr, M., Siskind, D. E., Drob, D. P., Picone, J. M., Stevens, M. H., Bailey, S. M., Bender, S., Bernath, P. F., Funke, B., Hervig, M. E., and Pérot, K.: NRLMSIS 2.1: An Empirical Model of Nitric Oxide Incorporated Into MSIS, *Journal of Geophysical Research: Space Physics*, 127, e2022JA030896, <https://doi.org/10.1029/2022JA030896>, 2022.
- ESA, S. D. O.: ESA's Annual Space Environment Report, Tech. rep., European Space Agency, Darmstadt, Germany, https://www.sdo.esoc.esa.int/environment_report/Space_Environment_Report_latest.pdf, 2025.
- Esposito, S., Scarabosio, A., Vecchi, G., and D'Ambrosio, D.: Non-equilibrium plasma distribution in the wake of a slender blunted-nose cone in hypersonic flight and its effect on the radar cross section, *Aerospace Science and Technology*, 155, 109 699, 2024.
- Evans, J. S. and Huber, P. W.: Calculated Radio Attenuation Due to Plasma Sheath on Hypersonic Blunt-Nosed Cone, Technical Note NASA TN D-2043, NASA, 1963.
- Fritts, D. C. and Alexander, M. J.: Gravity wave dynamics and effects in the middle atmosphere, *Reviews of geophysics*, 41, 2003.
- Grossir, G., Dias, B., Chazot, O., and Magin, T.: High temperature and thermal non-equilibrium effects on the determination of free-stream flow properties in hypersonic wind tunnels, *Physics of Fluids*, 30, 2018.
- Gustavsson, B.: AIDA_tools, https://github.com/BjornG-son/AIDA_tools, GitHub repository, accessed 2026-04-23, 2026.
- Gustavsson, B., Kosch, M., Wong, A., Pedersen, T., Heinselman, C., Mutiso, C., Bristow, B., Hughes, J., and Wang, W.: First estimates of volume distribution of HF-pump enhanced emissions at 6300 and 5577 Å: A comparison between observations and theory, in: *Annales Geophysicae*, vol. 26, pp. 3999–4012, Copernicus GmbH, 2008.

- Hankey, M., Perlerin, V., and Meisel, D.: The all-sky-6 and the Video Meteor Archive system of the AMS Ltd., *Planetary and Space Science*, 190, 105 005, 2020.
- He, X., Gao, C., and Jiang, T.: A Simplified Method for Calculating Spectral Emission of Nonequilibrium Air Plasmas in Hypersonic Shock-Layers, *Advances in Aerodynamics*, 3, 15, <https://doi.org/10.1186/s42774-021-00070-1>, 2021.
- Hersbach, H., Bell, B., Berrisford, P., Hirahara, S., Horányi, A., Muñoz-Sabater, J., Nicolas, J., Peubey, C., Radu, R., Schepers, D., et al.: The ERA5 global reanalysis, *Quarterly journal of the royal meteorological society*, 146, 1999–2049, 2020.
- Hersbach, H., Bell, B., Berrisford, P., Biavati, G., Horányi, A., Muñoz Sabater, J., Nicolas, J., Peubey, C., Radu, R., Rozum, I., Schepers, D., Simmons, A., Soci, C., Dee, D., and Thépaut, J.-N.: ERA5 hourly data on pressure levels from 1940 to present, <https://doi.org/10.24381/cds.bd0915c6>, accessed on 17-05-2026, 2023.
- Hupe, P., Pilger, C., Assink, J., Schneider, S., Näsholm, S. P., Grumer, J., Vierinen, J. P., Knach, D., Morfa, Y., Wing, R., Gerding, M., and Baumgarten, G.: Seismoacoustic analysis of a Falcon 9 rocket stage re-entry over central Europe on 19 February 2025, manuscript submitted to *Pure and Applied Geophysics*, 2025.
- Huyghebaert, D., Vierinen, J., Gustavsson, B., Latteck, R., Renkwitz, T., Zecha, M., Stephan, C. C., Conte, J. F., Kastinen, D., Kero, J., and Chau, J. L.: Monitoring of Lower Thermospheric Neutral Density Variations Using Meteor Head Echoes, *EGUosphere*, 2025, 1–16, <https://doi.org/10.5194/egusphere-2025-2323>, 2025.
- Kastinen, D., Kero, J., and Gritsevich, M.: Preparing for multi-modal measurements of meteors, part 1: AllSky7 and EISCAT_3D, *WGN, Journal of the International Meteor Organization*, 53, 46–50, 2025.
- Kim, M., Keidar, M., and Boyd, I. D.: Analysis of an electromagnetic mitigation scheme for reentry telemetry through plasma, *Journal of Spacecraft and Rockets*, 45, 1223–1229, 2008.
- Kruzynski, M., Zubowicz, T., Arminski, K., Karawacki, M., Teofilewicz, M., Wnuk, E., Aniol, Z., and Trocki, T.: The February 2025 re-entry event over Poland, in: *The Advanced Maui Optical and Space Surveillance (AMOS) Technologies Conference*, p. 109, 2025.
- Lin, S.-C.: Radio echoes from a manned satellite during re-entry, *Journal of Geophysical Research*, 67, 3851–3870, <https://doi.org/10.1029/JZ067i010p03851>, 1962.
- Lips, T., Fritsche, B., Koppenwallner, G., and Klinkrad, H.: Spacecraft destruction during re-entry—latest results and development of the SCARAB software system, *Advances in Space Research*, 34, 1055–1060, 2004.
- Maloney, C. M., Portmann, R. W., Ross, M. N., and Rosenlof, K. H.: Investigating the Potential Atmospheric Accumulation and Radiative Impact of the Coming Increase in Satellite Reentry Frequency, *Journal of Geophysical Research: Atmospheres*, 130, e2024JD042442, <https://doi.org/10.1029/2024JD042442>, 2025.
- McKinley, D. W. R.: *Meteor science and engineering*, New York, 1961.
- Miller, E. R.: *Scattering of Electromagnetic Waves from a Plasma-Immersed Cylinder*, Contractor Report NASA CR-86631, NASA, 1966.
- Mitchell, F., Mahaffey, W., and Jacob, R.: Modeling plasma effects on radar cross section of reentry vehicles, *IBM Journal of Research and Development*, 13, 468–474, 1969.
- Murphy, D. M., Abou-Ghanem, M., Cziczko, D. J., Froyd, K. D., Jacquot, J., Lawler, M. J., Maloney, C., Plane, J. M., Ross, M. N., Schill, G. P., et al.: Metals from spacecraft reentry in stratospheric aerosol particles, *Proceedings of the National Academy of Sciences*, 120, e2313374 120, <https://doi.org/10.1073/pnas.23133741>, 2023.
- Obenberger, K., Chau, J., Vierinen, J., Vida, D., Cordonnier, L., Balint, Z., Clahsen, M., Dao, E., Dowell, J., Holmes, J., et al.: First coincident radar and optical observations of a meteor radio afterglow, *Journal of Geophysical Research: Space Physics*, 131, e2025JA034 647, 2026.

- Oppenheim, M. M., Dyrud, L. P., and Vom Endt, A. F.: Plasma instabilities in meteor trails: 2-D simulation studies, *Journal of Geophysical Research: Space Physics*, 108, 2003.
- Peña-Asensio, E., Trigo-Rodríguez, J. M., Langbroek, M., Rimola, A., and Robles, A. J.: Using fireball networks to track more frequent reentries: Falcon 9 upper-stage orbit determination from video recordings, *Astrodynamics*, 5, 347–358, 2021.
- Petervari, R., Karl, S., Wagner, A., and Knott, P.: Radar Characterization of Hypersonic Wake Plasma in a High-Enthalpy Shock-Tunnel Flow: RCS, Micro-Doppler and Electron-Density Analysis, *Aerospace Science and Technology*, p. 111682, 2026.
- Poulter, E. and Baggaley, W.: Radiowave scattering from meteoric ionization, *Journal of Atmospheric and Terrestrial Physics*, 39, 757–768, 1977.
- Qian, J.-W., Zhang, H.-L., and Xia, M.-Y.: Modelling of Electromagnetic Scattering by a Hypersonic Cone-Like Body in Near Space, *International journal of antennas and propagation*, 2017, 3049 532, 2017.
- Rubin, G., Carney, T., Floyd, J., Henderson, H., Mitchell, J., Siegel, A., and Vila, J.: Airborne radar measurements of the reentry of the Ariane 5 EPC, in: *IEEE International Radar Conference*, 2005., pp. 469–473, IEEE, 2005.
- Scharfman, W. E. and Bredfeldt, H. R.: Use of the Langmuir probe to determine the electron density and temperature surrounding re-entry vehicles, *Contractor Report NASA 66275*, NASA, 1966.
- Schulz, L., Glassmeier, K.-H., Herberhold, M., Mitchell, A., Murphy, D. M., Plane, J. M. C., and Plaschke, F.: Space waste: An update of the anthropogenic matter injection into Earth's atmosphere, *Advances in Space Research*, 77, 9589–9616, <https://doi.org/10.1016/j.asr.2026.03.026>, 2026.
- Space Exploration Technologies Corp.: *Falcon User's Guide*, SpaceX, version 8 edn., applicable to Falcon 9 and Falcon Heavy launch vehicles, 2025.
- Turunen, E.: Incoherent scatter radar contributions to high latitude D-region aeronomy, *Journal of Atmospheric and Terrestrial Physics*, 58, 707–725, [https://doi.org/10.1016/0021-9169\(95\)00069-0](https://doi.org/10.1016/0021-9169(95)00069-0), 1996.
- Urco, J. M., Chau, J. L., Weber, T., Vierinen, J. P., and Volz, R.: Sparse signal recovery in MIMO specular meteor radars with waveform diversity, *IEEE Transactions on Geoscience and Remote Sensing*, 57, 10 088–10 098, 2019.
- Vierinen, J.: *Falcon9 data processing*, <https://github.com/jvierine/falcon9>, GitHub repository, accessed 2026-05-25, 2026a.
- Vierinen, J.: Replication Data for "Optical and VHF Radar Observations of the February 2025 Falcon 9 Upper- Stage Re-entry", <https://doi.org/10.5281/zenodo.20070800>, 2026b.
- Vierinen, J., Chau, J. L., Pfeffer, N., Clahsen, M., and Stober, G.: Coded continuous wave meteor radar, *Atmospheric Measurement Techniques*, 9, 829–839, 2016.
- Vierinen, J., Chau, J. L., Charuvil, H., Urco, J. M., Clahsen, M., Avsarkisov, V., Marino, R., and Volz, R.: Observing mesospheric turbulence with specular meteor radars: A novel method for estimating second-order statistics of wind velocity, *Earth and Space Science*, 6, 1171–1195, 2019.
- Vierinen, J., Aslaksen, T., Chau, J. L., Gritsevich, M., Gustavsson, B., Kastinen, D., Kero, J., Kozlovsky, A., Kværna, T., Midtskogen, S., et al.: Multi-instrument observations of the Pajala fireball: Origin, characteristics, and atmospheric implications, *Frontiers in astronomy and space sciences*, 9, 1027 750, 2022.
- Vondrak, T., Plane, J., Broadley, S., and Janches, D.: A chemical model of meteoric ablation, *Atmospheric Chemistry and Physics*, 8, 7015–7031, 2008.

- Wing, R., Gerding, M., Plane, J., Morfa, Y., Urco, J. M., Yamazaki, Y., Schulz, L., Höffner, J., Mielich, J., Renkwitz, T., et al.: Measurement of a Lithium Plume from the Uncontrolled Re-entry of a Falcon 9 Rocket, *Communications Earth & Environment*, 7, 161, <https://doi.org/10.1038/s43247-025-03154-8>, 2026.
- Younger, J., Lee, C., Reid, I., Vincent, R., Kim, Y., and Murphy, D.: The effects of deionization processes on meteor radar diffusion coefficients below 90 km, *Journal of Geophysical Research: Atmospheres*, 119, 10027–10043, 2014.